

# Comments Regarding Two Upwind Methods for Solving for Two-Dimensional External Flows Using Unstructured Grids

William L. Kleb \*

*NASA Langley Research Center, Hampton, Virginia, 23681*

## Introduction

Steady flow over the leading portion of a multicomponent airfoil section is studied using computational fluid dynamics (CFD) employing an unstructured grid. To simplify the problem, only the inviscid terms are retained from the Reynolds-averaged Navier-Stokes equations—leaving the Euler equations. The algorithm is derived using the finite-volume approach, incorporating explicit time-marching of the unsteady Euler equations to a time-asymptotic, steady-state solution. The inviscid fluxes are obtained through either of two approximate Riemann solvers: Roe's flux difference splitting or van Leer's flux vector splitting. Results are presented which contrast the solutions given by the two flux functions as a function of Mach number and grid resolution. Additional information is presented con-

---

\*Research Engineer, Aerothermodynamics Branch, Space Systems Division.

cerning code verification techniques, flow recirculation regions, convergence histories, and computational resources.

## Nomenclature

$A_{cell}$	Cell area
$a_k$	Wave speed
$c$	Speed of sound
$e$	Specific energy
$\mathbf{F}, \mathbf{G}$	Cartesian inviscid flux vectors
$h$	Specific enthalpy
$h_k$	Component of $\mathbf{H}$ vector
$\mathbf{H}$	Locally face-normal flux vector
$L_\infty$	Infinity error norm
$L_2$	Least-squares error norm
$M$	Mach number
$p$	Pressure
$\mathbf{R}$	Matrix of wave signature column vectors
$R_k$	Column vector component of $\mathbf{R}$
$\Delta s$	Length of cell side
$t$	Time
$\Delta t$	Time step
$\mathbf{T}$	Transformation matrix from Cartesian coordinates
$u, v$	Cartesian velocity components

$\mathbf{U}$	Conservative variables
$\Delta \mathbf{V}$	Wave strength vector of jumps
$x, y$	Cartesian coordinates to local normal/tangential coordinates
$\alpha_m$	Runge-Kutta coefficient
$\gamma$	Ratio of specific heats
$\theta$	Polar angle
$\nu$	Courant number
$\rho$	Density
$\Phi$	Flux function

## Subscripts

$( )_0$	Image cell value
$( )_1$	Interior cell value
$( )_k$	Vector component (k=1,2,3,4)
$( )_L$	States in the “left” cell
$( )_R$	States in the “right” cell
$( )_n$	Normal component
$( )_t$	Tangent component
$( )_\infty$	Freestream quantity

## Superscripts

$(\ )^n, (\ )^{n+1}$  Time levels

$(\ )^{\wedge}$  Roe-averaged quantity

$(\ )^*$  Smoothed values

$(\ )^+$  Right-traveling information

$(\ )^-$  Left-traveling information

## Governing Equations

Two-dimensional, unsteady flow is described by the following conservation laws

$$\frac{\partial}{\partial t}\mathbf{U} + \frac{\partial}{\partial x}\mathbf{F} + \frac{\partial}{\partial y}\mathbf{G} = \mathbf{0}$$

where the state vector is given by

$$\mathbf{U} = \begin{pmatrix} \rho \\ \rho u \\ \rho v \\ \rho e \end{pmatrix}$$

and the inviscid fluxes are

$$\mathbf{F} = \begin{pmatrix} \rho u \\ \rho u^2 + p \\ \rho uv \\ \rho uh \end{pmatrix} \quad \mathbf{G} = \begin{pmatrix} \rho v \\ \rho uv \\ \rho v^2 + p \\ \rho vh \end{pmatrix}$$

The equation of state closes the system

$$e = \frac{p}{(\gamma - 1)\rho} + \frac{1}{2}(u^2 + v^2)$$

and for convenience, enthalpy is defined as

$$h = e + \frac{p}{\rho}$$

Note: for air:  $\gamma = 1.4$ .

## Flux Functions

The inviscid fluxes were computed using two different upwind schemes: flux difference splitting (FDS) of Roe<sup>1</sup> and flux vector splitting (FVS) of van Leer.<sup>2</sup> Both techniques are outlined below.

## van Leer's Flux Vector Splitting

For van Leer's flux vector splitting scheme, the inviscid portion of the fluxes across a cell face is given by

$$\Phi(\mathbf{U}_L, \mathbf{U}_R) = \mathbf{T}^{-1} \left( \mathbf{H}^+(\mathbf{U}_L) + \mathbf{H}^-(\mathbf{U}_R) \right)$$

where  $\mathbf{T}^{-1}$  is the inverse transformation from cell face oriented coordinates to Cartesian coordinates

$$\mathbf{T}^{-1} = \begin{bmatrix} 1 & 0 & 0 & 0 \\ 0 & \sin\theta & \cos\theta & 0 \\ 0 & -\cos\theta & \sin\theta & 0 \\ 0 & 0 & 0 & 1 \end{bmatrix}$$

The fluxes are split into right-traveling and left-traveling based on the cell-centered, face-normal Mach number, i.e.,

$$M_n \geq 1 \quad \mathbf{H}^+ = \mathbf{H}(\mathbf{U}_L) \quad \mathbf{H}^- = \mathbf{0}$$

$$M_n \leq -1 \quad \mathbf{H}^+ = \mathbf{0} \quad \mathbf{H}^- = \mathbf{H}(\mathbf{U}_R)$$

$$|M_n| < 1 \quad \mathbf{H}^+ = \mathbf{H}^+(\mathbf{U}_L) \quad \mathbf{H}^- = \mathbf{H}^-(\mathbf{U}_R)$$

where

$$\mathbf{H}(\mathbf{U}) = \begin{pmatrix} \rho u_n \\ \rho u_n^2 + p \\ \rho u_n u_t \\ \rho u_n h \end{pmatrix}$$

and

$$\mathbf{H}^{\pm}(\mathbf{U}) = \begin{pmatrix} h_1^{\pm} \\ h_2^{\pm} \\ h_3^{\pm} \\ h_4^{\pm} \end{pmatrix} = \begin{pmatrix} \pm \frac{1}{4} \rho c (M_n \pm 1)^2 \\ h_1^{\pm} c [(\gamma - 1) M_n \pm 2] / \gamma \\ h_1^{\pm} c M_t \\ \left[ h_2^{\pm 2} \frac{\gamma^2}{2(\gamma^2 - 1)} + \frac{h_3^{\pm 2}}{2} \right] / h_1^{\pm} \end{pmatrix}$$

### Roe's Flux Difference Splitting

For Roe's flux difference splitting scheme, the flux is given as a central difference term in addition to a dissipation term,

$$\Phi(\mathbf{U}_L, \mathbf{U}_R) = \frac{1}{2} [\Phi(\mathbf{U}_L) + \Phi(\mathbf{U}_R)] - \frac{1}{2} \sum_{k=1}^4 |\hat{a}_k|^* \Delta V_k \hat{R}_k$$

where the wave speeds are

$$\hat{\mathbf{a}} = \begin{pmatrix} \hat{u}_n - \hat{c} \\ \hat{u}_n \\ \hat{u}_n \\ \hat{u}_n + \hat{c} \end{pmatrix}$$

the jumps in the wave strengths are

$$\Delta \mathbf{V} = \begin{pmatrix} \frac{\Delta p - \hat{\rho} \hat{c} \Delta u_n}{2 \hat{c}^2} \\ \frac{\hat{\rho} \Delta u_t}{\hat{c}} \\ \frac{\Delta \rho \hat{c}^2 - \Delta p}{\hat{c}^2} \\ \frac{\Delta p + \hat{\rho} \hat{c} \Delta u_n}{2 \hat{c}^2} \end{pmatrix}$$

and the wave signatures are given by

$$\begin{aligned}\hat{\mathbf{R}} &= \begin{pmatrix} \hat{R}_1 & \hat{R}_2 & \hat{R}_3 & \hat{R}_4 \end{pmatrix} \\ &= \begin{pmatrix} 1 & 0 & 1 & 1 \\ \hat{u} - \hat{c} \sin\theta & \hat{c} \cos\theta & \hat{u} & \hat{u} + \hat{c} \sin\theta \\ \hat{v} + \hat{c} \cos\theta & \hat{c} \sin\theta & \hat{v} & \hat{v} - \hat{c} \cos\theta \\ \hat{h} - \hat{u}_n \hat{c} & \hat{u}_t \hat{c} & \frac{1}{2}(\hat{u}^2 + \hat{v}^2) & \hat{h} + \hat{u}_n \hat{c} \end{pmatrix}\end{aligned}$$

where  $\Delta(\ )$  represents the jump between the left and right states

$$\Delta(\ ) = (\ )_R - (\ )_L$$

and the  $(\hat{\ })$  quantities are the Roe-averaged variables

$$\begin{aligned}\hat{\rho} &= \sqrt{\rho_L \rho_R} \\ \hat{u} &= \frac{\sqrt{\rho_L} u_L + \sqrt{\rho_R} u_R}{\sqrt{\rho_L} + \sqrt{\rho_R}} \\ \hat{v} &= \frac{\sqrt{\rho_L} v_L + \sqrt{\rho_R} v_R}{\sqrt{\rho_L} + \sqrt{\rho_R}} \\ \hat{h} &= \frac{\sqrt{\rho_L} h_L + \sqrt{\rho_R} h_R}{\sqrt{\rho_L} + \sqrt{\rho_R}}\end{aligned}$$

where  $\hat{c}$ ,  $\hat{u}_n$ , and  $\hat{u}_t$  are calculated directly from  $\hat{\rho}$ ,  $\hat{u}$ ,  $\hat{v}$ , and  $\hat{h}$ , so

$$\hat{p} = \frac{(\gamma - 1)\hat{\rho}}{\gamma} \left[ \hat{h} - \frac{1}{2}(\hat{u}^2 + \hat{v}^2) \right]$$



$$\hat{c} = \sqrt{\frac{\gamma \hat{p}}{\hat{\rho}}}$$

$$\hat{u}_n = \hat{u} \sin \theta - \hat{v} \cos \theta$$

$$\hat{u}_t = \hat{u} \cos \theta + \hat{v} \sin \theta$$

To prevent expansion shocks, an entropy fix is imposed. A smoothed value of  $|\hat{a}_k|$  is defined for the acoustic waves (  $k = 1$  and  $k = 4$  )

$$|\hat{a}_k|^* = \begin{cases} |\hat{a}_k| & |\hat{a}_k| \geq \frac{1}{2} \delta a_k \\ \frac{\hat{a}_k^2}{\delta a_k} + \frac{1}{4} \delta a_k & |\hat{a}_k| < \frac{1}{2} \delta a_k \end{cases}$$

with

$$\delta a_k = \max(4\Delta a_k, 0)$$

This provides a parabolic (and thus continuous) curve where the wave speeds change signs (*e.g.*, in a transonic expansion, or at a stagnation point).

## Time Integration

Time integration of the governing equations was performed by two methods: forward Euler and Runge-Kutta, with the time step per cell area was computed via

$$\frac{\Delta t}{A_{cell}} = \frac{\nu}{\max_{faces} [(u_n + c) \Delta s]}$$

where  $\nu$  is the Courant number.

## Forward Euler

The simplest scheme is that of forward Euler

$$\mathbf{U}^{n+1} = \mathbf{U}^n - \frac{\Delta t}{A_{cell}} \mathbf{R}(\mathbf{U}^n)$$

where  $\mathbf{R}$  is the residual of the cell given by

$$\mathbf{R}(\mathbf{U}^n) = \sum_{faces} \Phi \Delta s$$

This scheme was only used as a step in the debugging process enroute to the following multi-stage scheme.

## Runge-Kutta

A four-stage, optimally-smoothing, Runge-Kutta, time-stepping scheme due to Tai<sup>3</sup> was implemented as follows

$$\begin{aligned} \mathbf{U}^0 &= \mathbf{U}^n \\ \mathbf{U}^1 &= \mathbf{U}^0 - \alpha_1 \frac{\Delta t}{A_{cell}} \mathbf{R}(\mathbf{U}^0) \\ \mathbf{U}^2 &= \mathbf{U}^0 - \alpha_2 \frac{\Delta t}{A_{cell}} \mathbf{R}(\mathbf{U}^1) \\ \mathbf{U}^3 &= \mathbf{U}^0 - \alpha_3 \frac{\Delta t}{A_{cell}} \mathbf{R}(\mathbf{U}^2) \\ \mathbf{U}^4 &= \mathbf{U}^0 - \alpha_4 \frac{\Delta t}{A_{cell}} \mathbf{R}(\mathbf{U}^3) \\ \mathbf{U}^{n+1} &= \mathbf{U}^4 \end{aligned}$$

with  $\alpha_k = [0.0833, 0.2069, 0.4265, 1.0]$ . The scheme was nominally run with a Courant number of 2.0.

## Boundary Conditions

The solid wall boundary condition for the airfoil was enforced in a weak sense by setting the cell-centered state in an image-cell located just inside the solid boundary surface. Physically, flow tangency must be preserved at the wall, as well as a zero pressure gradient normal to the wall. This image-cell wall-boundary procedure is of first order accuracy, because it neglects the wall curvature. This will introduce inaccuracy in the case of a highly curved wall that is not resolved by sufficiently fine cells on the wall. This defines the values in the image-cell as follows

$$\rho_0 = \rho_1$$

$$p_0 = p_1$$

$$(u_t)_0 = (u_t)_1$$

$$(u_n)_0 = -(u_n)_1$$

where the  $(\ )_0$  represents an image-cell quantity and  $(\ )_1$  is the appropriate interior cell quantity. The flow tangency condition is supplied by merely reflecting the normal component of velocity across the boundary face. In more realistic terms, this boundary condition can be thought of as a symmetry-plane condition.

For the farfield boundary, the image-cells were specified as freestream conditions, and the Riemann solver simply picks the proper information to use depending on whether the

local flow is into or out-of the computational domain. Note: a more careful outer boundary condition for a lifting airfoil would superimpose a potential vortex velocity field at the outer boundary.

## Computational Meshes

Three different sizes of meshes were used for this project as indicated in Table 1. The results were computed on the medium grid unless otherwise specified. Figure 1 shows a view of each of the grids in the vicinity of the airfoil.

## The Debugging Process

Debugging the code is the most labor intensive part of any project—if it is not done in a logical manner. Steps along the debugging path were as follows:

1. Check pointers for a simple mesh.
2. Verifying cell areas were positive and correct magnitude.
3. Implement only forward Euler time stepping.
4. Setting all boundary conditions to be freestream conditions.
5. Verify both flux functions agree with one another.
6. Run angle of attacks:  $0^\circ, \pm 45^\circ, \pm 90^\circ$ .
7. Add solid wall boundary conditions.
8. Run angle of attacks:  $0^\circ, \pm 45^\circ, \pm 90^\circ$ .

9. Turn on the multistage time stepping.
10. Run angle of attacks:  $0^\circ, \pm 45^\circ, \pm 90^\circ$ .
11. A freestream Mach of 2.5 was run to determine (very readily) that the flow was going in the right direction—indicated by a very pronounced bow shock encompassing the front of the body.
12. A grid convergence study was conducted to check for consistency of the algorithm—see following section.

The final check was done just from knowledge of how the flow should behave—common sense.

## Results and Discussion

The flow over the leading section of a multicomponent airfoil is computed for three different freestream Mach numbers: 0.4, 0.8, and 1.2. The Mach 0.8 case was arbitrarily chosen for a grid convergence study, and it was run on all three meshes: coarse, medium, and fine. Each Mach number/grid combination was also run using both of the flux functions discussed previously.

### Computational Resources

The code was primarily run on a Hewlett Packard Apollo series 700 workstation. When compiler-optimized, the code typically ran around  $2.6 \times 10^{-4}$  CPUs/iteration/cell when using the FDS flux function. For example, a 6124 cell mesh running for 2200 iterations would have a total CPU time of around 1 hour. Timings for different machines and flux functions are

given in Table 2. As coded, the FVS scheme runs 40 percent faster than the FDS scheme. Note that the Sun Sparc station runs an order of magnitude slower than either of the HPs.

### **Mach Number Effects**

Figure 2 depicts Mach contours of the flow in the vicinity of the airfoil for three Mach numbers: 0.4, 0.8, and 1.2. The sonic line and the  $M = 0.5$  contour lines are labeled in each subfigure. The remaining contour lines occur at intervals of 0.1 Mach. The results in the left column of the figure were produced using Roe's FDS flux function and those in the right column resulted from van Leer's FVS flux function. Comparing the left and right columns of Fig. 2 it is apparent that the two different flux functions give nearly identical results for the flow field. The only differences are minor and occur in the trailing edge/flap cavity region which will be investigated further in the following section. The Mach 0.4 case shows a stagnation region at the leading edge followed by two expansions: one near the leading edge on the suction side of the airfoil and another just before the flap slot on the pressure side. The Mach 0.8 flow contains two shocks: a strong one on the upper surface around 90 percent chord and a smaller one following a transonic expansion in the flap cavity. There is also a significant supersonic "bubble" on the upper surface. At Mach 1.2, the upper surface shock moves to the trailing edge and forms the familiar "fish-tail" shock structure. Also apparent is a weak, detached bow shock standing well off the leading edge.

### **Flap Cavity Region**

The differences between the two flux functions become more apparent upon closer inspection of the flap cavity region. Figure 3 shows streamlines around the trailing portion of the airfoil for a freestream Mach of 0.8 on all three grids for both flux functions. The figure

shows the results using Roe’s FDS in the left column and results using van Leer’s FVS in the right column. Notice that for all three grids, FDS shows a vortical structure in the flap region, while FVS only shows a vortical structure for the two finer grids. In addition, FDS supports a much more complex structure—the fine mesh showing three interacting recirculation regions. This is a result of the lower dissipation inherent in Roe’s FDS scheme as compared to van Leer’s FVS scheme.

### **Grid Convergence**

Shown in Fig. 4 are Mach number contours about the airfoil for three different grids. The flow has a freestream Mach number of 0.8 and was computed using the FDS flux function. As portrayed in the Fig. 4, the global solution only changes with respect to the thickness of the shock, implying that the scheme is consistent with respect to the governing equations.

### **Convergence Histories**

A summary of the total number of iterations required to reach an  $L_2$  error norm of the energy equation of  $1.0 \times 10^{-6}$  is shown in Table 3. Roe’s FDS scheme takes longer to converge than van Leer’s FVS scheme in every case. This is apparently due to the highly dissipative nature of FVS which tends to smooth spurious transients. In two cases, the FDS scheme even fails to converge to the specified error tolerance—more on this to follow.

Shown in Fig. 5 are normalized convergence histories for three different Mach numbers using the two flux functions. (Note: the straight line at the tail of the iteration line-plots is an artifact of the plotting routine used.) This figure clearly shows the convergence problem inherent in this application of Roe’s FDS flux function. Notice the cyclic behavior of the error residual. This corresponds to the following cycle: a flow feature moving just slightly,

the disturbance propagating into the rest of the field, and a reflected disturbance telling the feature to move back. The process repeats with a cycle corresponding to speed of the disturbance and the number of cells through which it passes. This was verified by halving the Courant number and noting a increase by a factor of two in the cycle period—the shape remained the same.

Shown in Fig. 6 and Fig. 7 are the regions which contained the most  $L_\infty$  error norms during the run for each of two cases. The left side of each figure is a blocked-contour plot of the number of times a particular cell was responsible for the  $L_\infty$  error norm. The right side of the figures shows the streamlines in the same viewing area. Figure 6 corresponds to a Mach 0.8 flow using the fine grid and Fig. 7 corresponds to a Mach 1.2 flow using the medium grid. For the Mach 0.8 case, the flow features responsible for the convergence problem appears to be both the transonic expansion on the bottom edge of the flap cavity region and the shock standing on the upper surface of the airfoil. However, in the Mach 1.2 case, the flow feature responsible for the convergence problem is the shock just ahead of the recirculation zone in the center of the airfoil flap cavity region.

An attempt was made to alleviate the convergence problem by “smoothing” the grid slightly. This was done by telling each node to move toward the centroid formed by its neighbors. This smoothing process altered the grid enough to stabilize the flow features in slightly different locations—hopefully allowing convergence; but the residual just hung at a slightly lower error norm.



## Conclusion

The results indicate that an airfoil experiences radically different flow fields as a function of Mach number. Features range from smooth variations of the flow properties at a low Mach numbers to discontinuous shocks forming at higher Mach numbers. In spite of the range of flow conditions, both flux functions appear to work quite well. Even though FDS is slightly more expensive than FVS *and* it experiences convergence difficulties, it appears to do a better job resolving recirculation regions than does FVS.

## References

- <sup>1</sup>Roe, P. L., “Approximate Riemann Solvers, Parameter Vectors, and Difference Schemes,” *Journal of Computational Physics*, vol. 43, pp. 357–372, October 1981.
- <sup>2</sup>van Leer, B., “Flux Vector Splitting for the Euler Equations,” *Lecture Notes in Physics*, pp. 507–512, July 1982.
- <sup>3</sup>Tai, C. H., *Acceleration Techniques for Explicit Euler Codes*. PhD thesis, University of Michigan, 1990.

**Table 1:** Mesh statistics

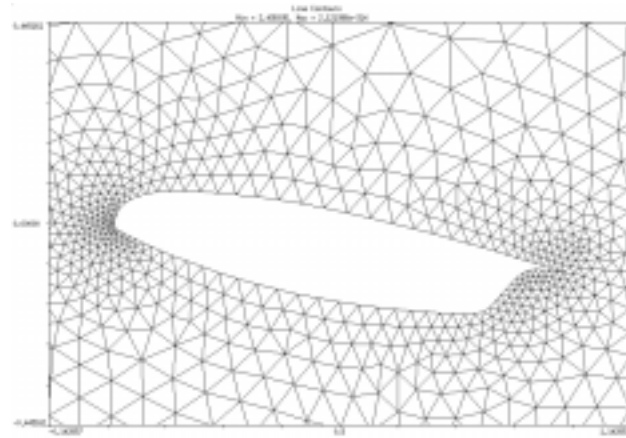
Name	Cells	Edges	Nodes
coarse	2697	4098	1401
medium	4025	6114	2089
fine	6124	9308	3184

**Table 2:** CPU seconds per iteration per cell

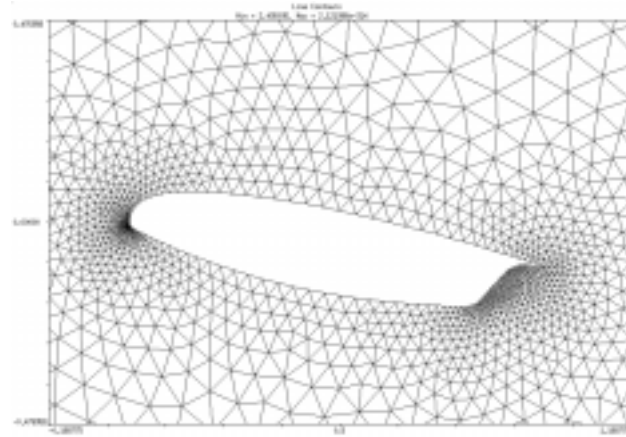
Machine	FDS	FVS
Sun Sparc 1+	$3.9 \times 10^{-3}$	$1.4 \times 10^{-3}$
HP Apollo 710	$2.6 \times 10^{-4}$	$1.8 \times 10^{-4}$
HP Apollo 720	$2.5 \times 10^{-4}$	$1.7 \times 10^{-4}$

**Table 3:** Number of iterations for convergence

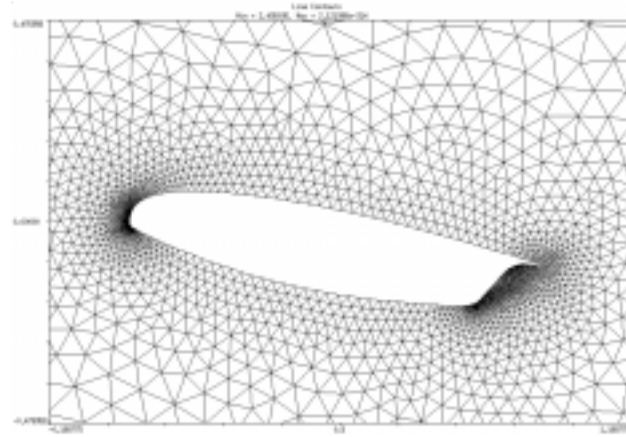
Mach	Grid	FDS	FVS
0.4	medium	2542	2123
0.8	coarse	1738	1496
	medium	2733	1909
	fine	hung	2396
1.2	medium	hung	1823



(a) Course grid.

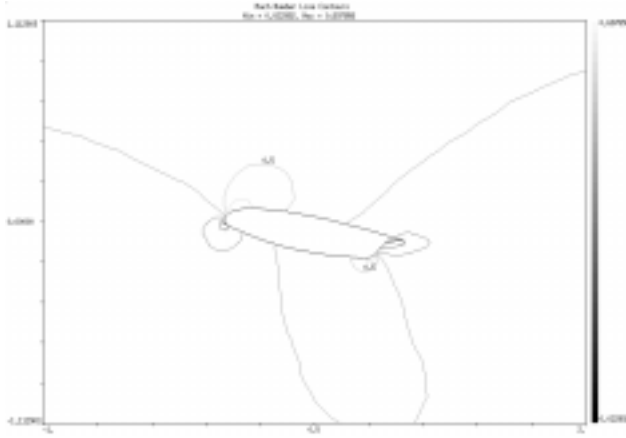


(b) Medium grid.

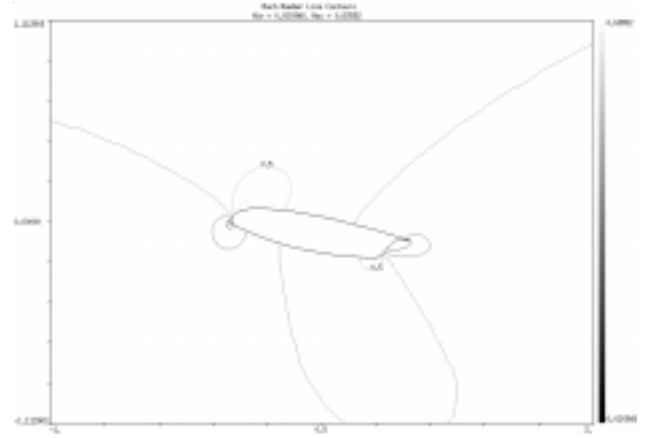


(c) Fine grid.

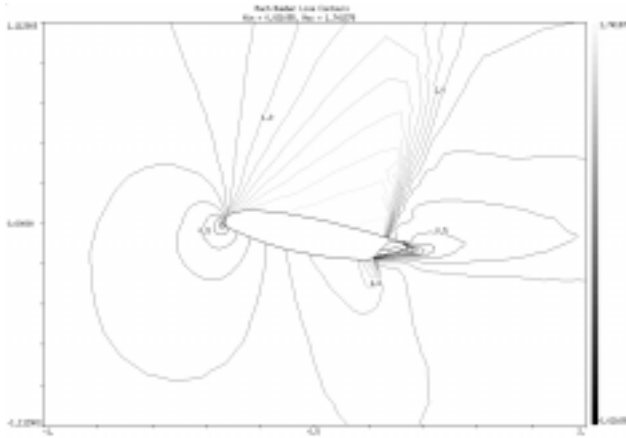
**Figure 1:** Computational meshes employed.



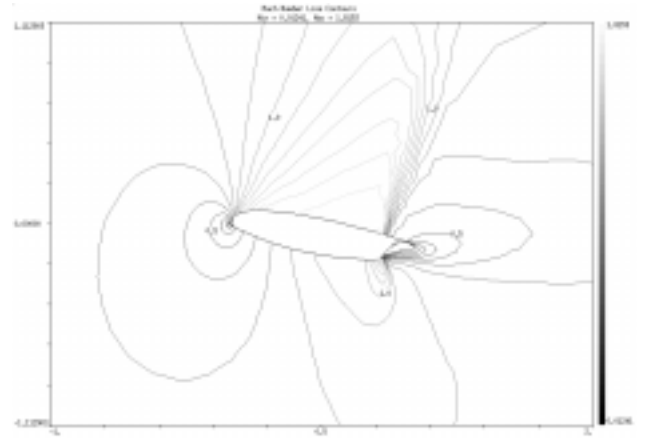
(a) Mach 0.4 FDS.



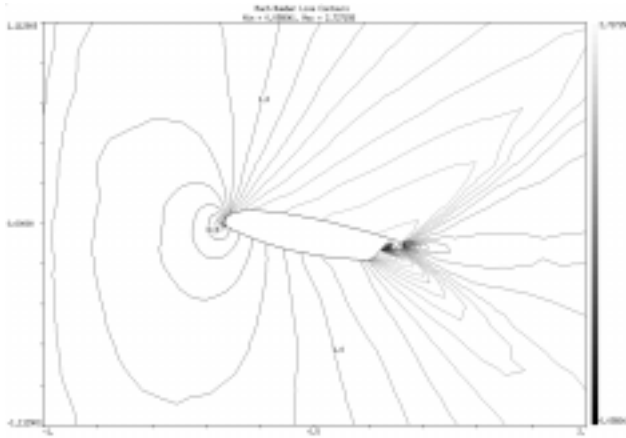
(b) Mach 0.4 FVS.



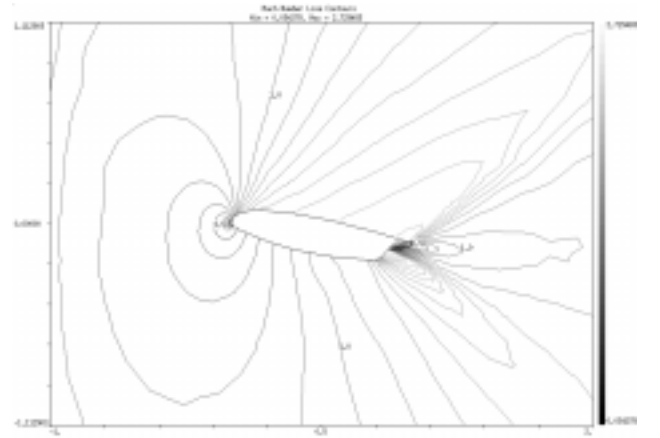
(c) Mach 0.8 FDS.



(d) Mach 0.8 FVS.

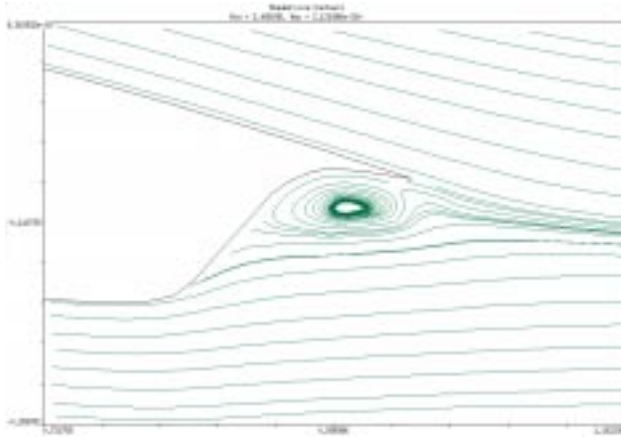


(e) Mach 1.2 FDS.

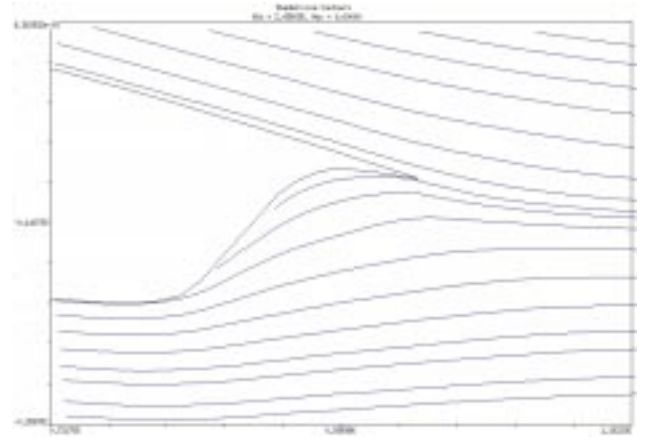


(f) Mach 1.2 FVS.

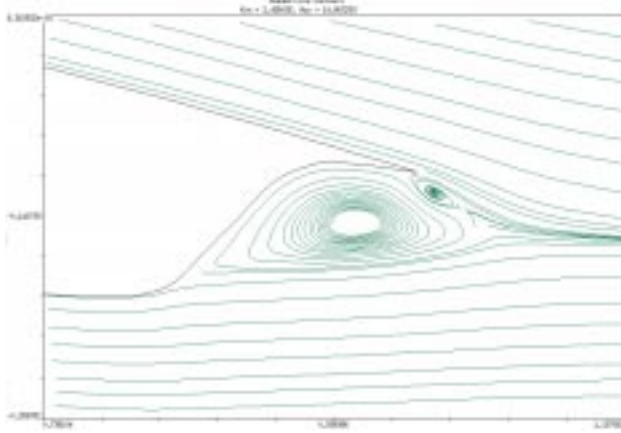
**Figure 2:** Comparison of Mach number contours for three Mach numbers ( $\Delta M = 0.1$ ).



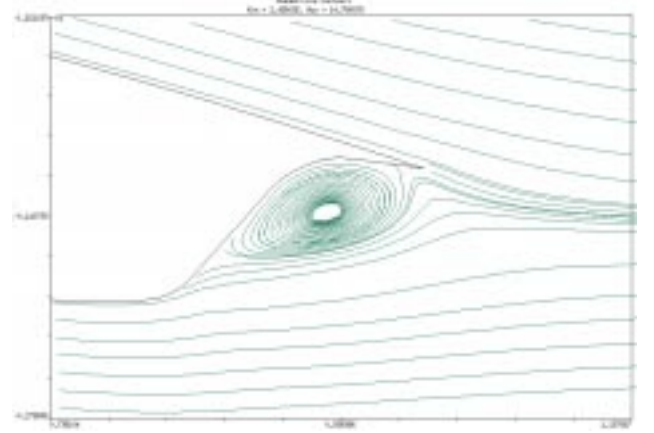
(a) Coarse grid, FDS.



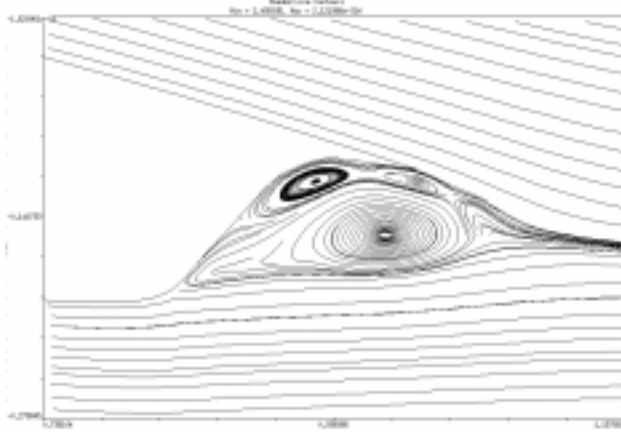
(b) Coarse grid, FVS.



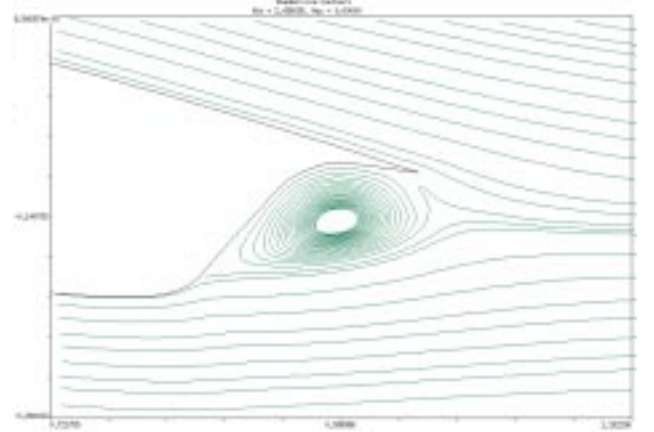
(c) Medium grid, FDS.



(d) Medium grid, FVS.

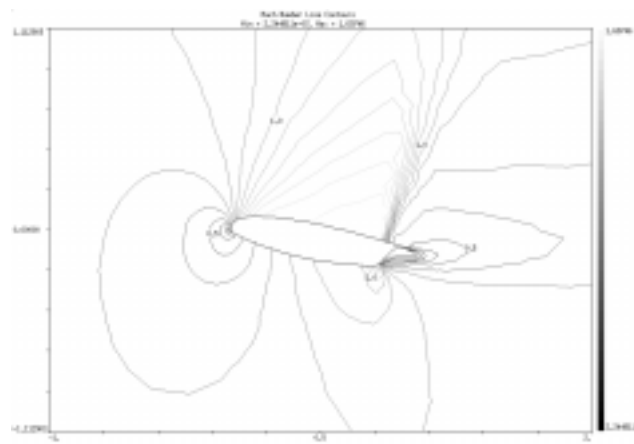


(e) Fine grid, FDS.

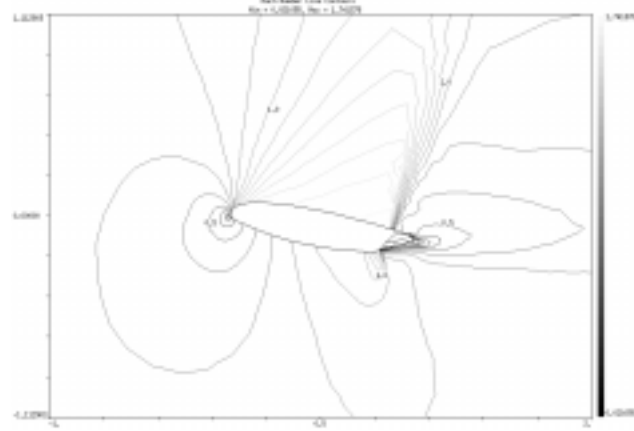


(f) Fine grid, FVS.

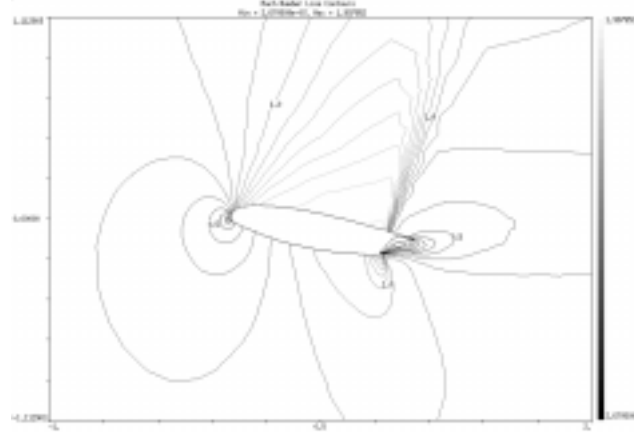
**Figure 3:** Streamline comparison for the flap cavity region of the airfoil using three different grids.



(a) Course grid.



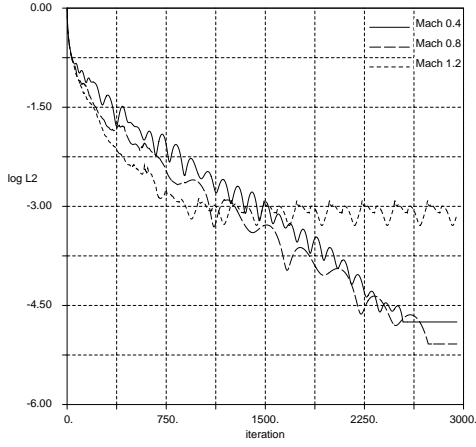
(b) Medium grid.



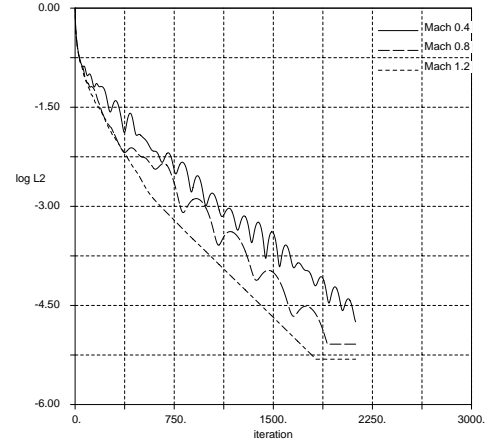
(c) Fine grid.

**Figure 4:** Comparison of Mach number contours for  $M_\infty = 0.8$  on three different grids ( $\Delta M = 0.1$ ).

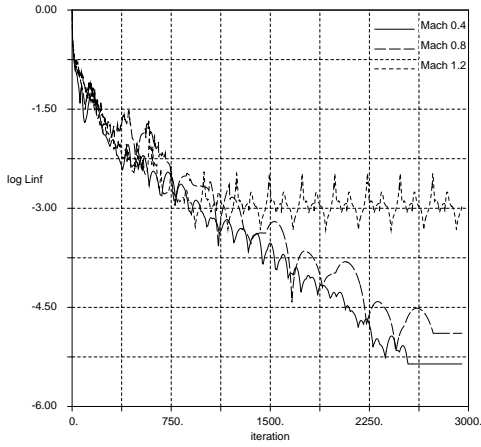




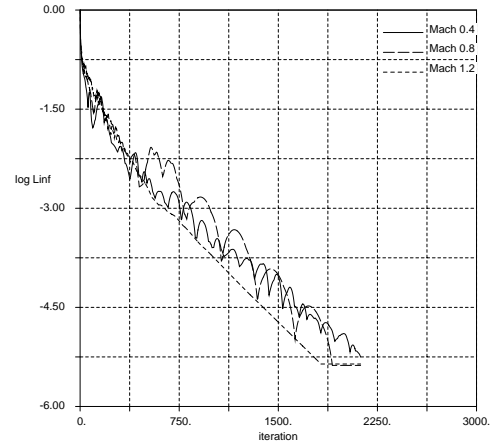
(a)  $L_2$  error norm FDS.



(b)  $L_2$  error norm FVS.

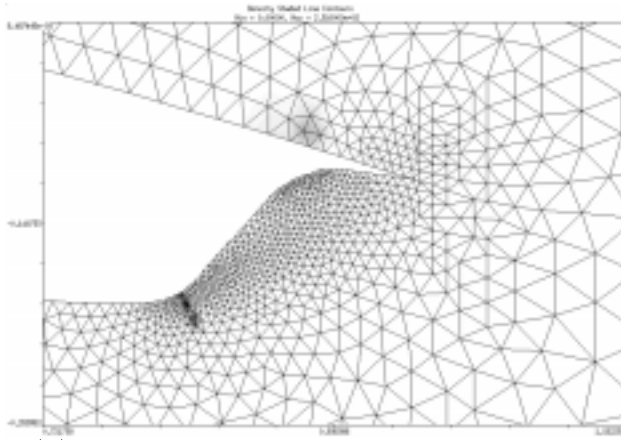


(c)  $L_\infty$  error norm FDS.

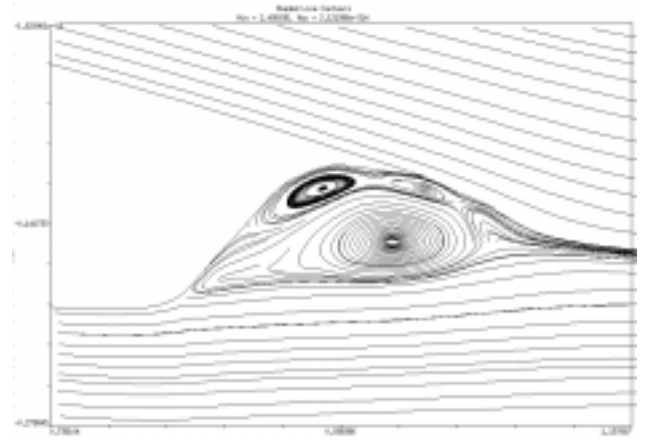


(d)  $L_\infty$  error norm FVS.

**Figure 5:** Normalized convergence histories for three Mach numbers.

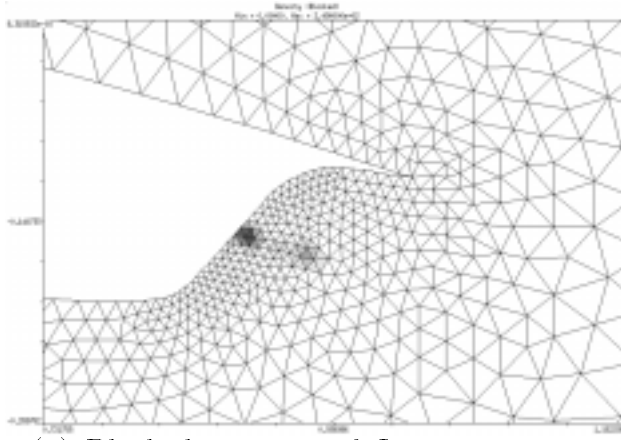


(a) Blocked-contours of  $L_\infty$  norm occurrences.

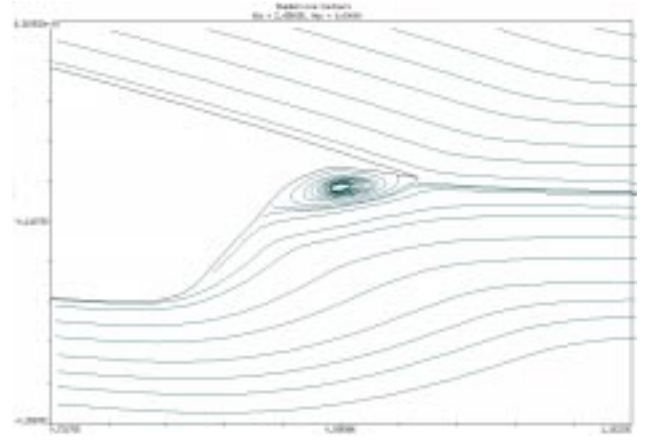


(b) Streamlines in the same vicinity.

**Figure 6:** Regions responsible for the convergence difficulties of FDS scheme at Mach 0.8, fine grid.



(a) Blocked-contours of  $L_\infty$  norm occurrences.



(b) Streamlines in the same vicinity.

**Figure 7:** Regions responsible for the convergence difficulties of FDS scheme at Mach 1.2, medium grid.